

Single-step solution combustion synthesis of porous 1393-B3 glass powders and structural characterization via solid-state NMR spectroscopy

Mehrnoosh Ghanad^{a,1}, Negar Akrami^{a,1}, Philipp Keil^b, Henrik Bradtmüller^{c,**}, Michael Ryan Hansen^b, Jalil Vahdati Khaki^a, Sahar Mollazadeh Beidokhti^{a,*}

^a Department of Materials Engineering, Faculty of Engineering, Ferdowsi University of Mashhad (FUM), Azadi Sq, Mashhad, Iran

^b Institute of Physical Chemistry, WWU Münster, Corrensstraße 28/30, D-41849, Münster, Germany

^c Department of Materials Engineering, Vitreous Materials Laboratory, Federal University of São Carlos, CP 676, 13565-905, São Carlos, SP, Brazil

ARTICLE INFO

Handling Editor: P. Vincenzini

Keywords:

Glass
Solution combustion synthesis
Nanoporous
NMR

ABSTRACT

During the last few decades, considerable progress has been made in designing novel boron-containing bio-glasses for soft tissue regeneration applications. For this purpose, conventional glass synthesis procedures such as melt-quenching and sol-gel synthesis have been explored extensively. However, both methods are time and energy-consuming and need expensive materials and equipment. The current study demonstrates that straightforward and low-cost solution combustion synthesis (SCS) can produce highly porous 1393-B3 borate-based glasses employing urea and sucrose as novel fuels. Thermal analysis shows that the glass transition temperatures of the produced specimens are between 650 and 680 °C. The X-ray diffraction (XRD) and field emission scanning electron microscopy (FESEM) methods were used to confirm the absence of crystalline impurity phases and to show the highly porous microstructure of the glasses, respectively. The effect of the initial temperature of the combustion area (T_0) on the glass structure of the obtained powders was investigated in detail via vibrational and NMR spectroscopies. The results indicate that optimum T_0 values are achieved at temperatures ranging from 500 to 700 °C using urea and 400–750 °C using sucrose as fuels. Increasing the temperature beyond these limits results in the partial devitrification of the parent glass. FT-IR, Raman, ¹¹B MAS, and 3QMAS NMR spectroscopies demonstrate that the glass structure is dominated by multiple distinct BO₄ and BO₃ units, i.e., neutral (B³ⁿ) and anionic (B^{3a}, B⁴) borate units. Increasing T_0 values reduce the fraction of the four-coordinated boron (N_4) from about 60 to 35% under the transformation of B⁴ units into B^{3a} units, while the overall amount of neutral B³ species stays nearly constant. The possibility of fine-tuning the boron speciation in the resulting glasses through the synthesis parameters demonstrates that SCS is a promising process for the scalable production of 1393-B3 glass powders with tailored physical properties.

1. Introduction

Numerous studies have been conducted over the past 20 years on bioactive glasses' development, manufacturing, and characterization [1]. The first bioactive glass composition was the silicate-based 45S5 glass introduced by L. Hench in the late 1960s, which has been utilized in various real-world medical applications recently [2]. Since then, substantial efforts have been made to find further bio-glass formulations

for hard and soft tissue regeneration [3]. Borate-based bioactive glasses have been the center of attention in various studies for soft tissue healing applications because of their beneficial biological activity, biocompatibility, and restoration properties [4]. Recent research showed that boron deficiency in the human body reduces bone volume and trabecular thickness and results in malign bone abnormalities [5]. Accordingly, boron supplementation can impact the incitement of wound healing *in vivo*, the release of growth factors and cytokines, the enhancement of

* Corresponding author. Department of Materials Engineering, Faculty of Engineering, Ferdowsi University of Mashhad (FUM), Azadi Square, Mashhad, Razavi Khorasan Province, Iran.

** Corresponding author. Vitreous Materials Laboratory (LaMaV), Department of Materials Engineering (DEMa), Federal University of São Carlos (UFSCar), Rod. Washington Luis, km 235 C.P. 676, 13.565-905, São Carlos, SP, Brazil.

E-mail addresses: mehrnooshghanad@gmail.com (M. Ghanad), akraminegar@gmail.com (N. Akrami), philipp.keil@uni-muenster.de (P. Keil), mail@bradtmueller.net (H. Bradtmüller), mhansen@uni-muenster.de (M.R. Hansen), vahdati@um.ac.ir (J.V. Khaki), mollazadeh.b@um.ac.ir (S.M. Beidokhti).

¹ These authors contributed equally.

<https://doi.org/10.1016/j.ceramint.2023.01.061>

Received 13 June 2022; Received in revised form 12 December 2022; Accepted 7 January 2023
0272-8842/© 20XX

RNA synthesis, and the development of extracellular matrix turnover [6]. It has been shown that bioactive borate glasses are suitable candidates for boron delivery in the human body [5]. Furthermore, due to their high solubility, borate bioactive glasses form hydroxyapatite (HA) faster than silicate-based bio-glasses [7,8]. Consequently, the rapid and controllable chemical reactions of borate-based bio-glasses with the surrounding environment led to studies focusing on the applications of mentioned borate glasses for soft tissue regeneration [9,10] (see Table 8).

The most well-known bio-glasses are typically produced through conventional routes via melt-quenching or sol-gel methods. Melt-quenching procedures, however, suffer from significant challenges for large-scale production, such as requiring costly crucibles and high-temperature furnaces [11–14]. On the other hand, while the sol-gel method overcomes some of these problems, as it requires lower synthesis temperatures and provides the opportunity of producing glasses with increased surface area, nano-porosity, and homogeneity [15]. However, stabilization of the sol and achieving good reproducibility is often rather complicated, and requires significant chemical expertise [16]. For bioglass manufacturing, synthesis in short periods without repeating heat treatment processes is critical. In addition, attaining bio-glasses with remarkable structural homogeneity, especially for glass compositions containing components with high chemical affinity, is challenging. An example of recent efforts to overcome the mentioned limitations is the preparation of bioglasses through citric acid-assisted sol-gel synthesis coupled with a self-propagating combustion method (SPC) [17]. Although the introduced synthesis method is intriguing, the preparation process of the two-step SPC method still requires a lot of time; thus, there is still further scope for future improvement.

The solution-combustion synthesis (SCS) method, traditionally used to prepare bio-ceramics, appears promising for solving the challenges mentioned earlier [18]. The synthesis process consists of fast and self-sustained exothermic reactions between the fuel(s) and oxidizer(s) [19] and is capable of producing complex homogeneous structures at low temperatures in a short period of time [18]. Using this method for the synthesis of different powders provides several benefits: (1) producing homogeneous nano-porous powders from cheap raw materials through the short and exothermic combustion reaction releasing a high volume of gaseous by-products; (2) manipulating the physiochemical properties of the final synthesized powders by controlling the ratio between chemical precursors and fuel(s) and T_0 [19–22]. (3) self-sustaining reaction with immediate response capabilities; and (4) high yields suitable for large-scale production [20,23].

In light of the above, the present research discusses the preparation of 13–93 borate-based glass powders (1393-B3) through single-step SCS for the first time. The effects of varying T_0 and fuel types on the physicochemical properties of the produced glass powders were investigated via thermal analysis. Moreover, the structure of the resulting glass powders was investigated through a comprehensive structural study employing X-Ray diffraction (XRD), vibrational- (FTIR and Raman), and NMR spectroscopies. The obtained results give insights into the synthesis-temperature/structure relationship of the borate glass network and demonstrate the feasibility of obtaining bioglass powders via the SCS method.

2. Materials and methods

2.1. Sample preparation

Borate-based 1393-B3 glass powders, with a nominal composition of $54.6\text{B}_2\text{O}_3\text{--}6\text{Na}_2\text{O--}7.9\text{K}_2\text{O--}7.7\text{MgO--}22.1\text{CaO--}1.7\text{P}_2\text{O}_5$, were synthesized using solution combustion synthesis based on the general procedures described elsewhere [19–22]. Appropriate amounts of the nitrate salt precursors, listed in Table 1, were dissolved in 5 cm^3 of deionized water. H_3BO_3 and H_3PO_4 were then added to the solution and thor-

Table 1
Raw materials employed for the synthesis of 1393-B3 glass powders.

Compound name	Chemical formula	Supplier	Purity (%)
Phosphoric acid 85%	H_3PO_4	Sigma-Aldrich, USA	$\geq 99.99\%$
Boric acid	H_3BO_3	Sigma-Aldrich, USA	$\geq 99.50\%$
Calcium nitrate tetrahydrate	$\text{Ca}(\text{NO}_3)_2 \cdot 4\text{H}_2\text{O}$	Sigma-Aldrich, USA	$\geq 99.00\%$
Magnesium nitrate hexahydrate	$\text{Mg}(\text{NO}_3)_2 \cdot 6\text{H}_2\text{O}$	Sigma-Aldrich, USA	99.00%
Potassium nitrate	KNO_3	Sigma-Aldrich, USA	$\geq 99.00\%$
Sodium nitrate	NaNO_3	Sigma-Aldrich, USA	$\geq 99.00\%$
Urea	NH_2CONH_2	Sigma-Aldrich, USA	$\geq 99.00\%$
Sucrose	$\text{C}_{12}\text{H}_{22}\text{O}_{11}$	Sigma-Aldrich, USA	$\geq 99.50\%$

oughly stirred for at least 1 h to obtain a homogeneous, and concentrated final solution. Urea was added to one part of the final solutions so that a fuel-to-oxidizer ratio of $\varphi = 1$ was attained and sucrose to the other part with a fuel-to-oxidizer ratio of $\varphi = 0.84$, according to the chemical reactions of (E1S) and (E2S), (Appendix Section). The reaction mixtures were then mixed for another 30 min and subsequently placed and held in pre-heated box furnaces at 400, 500, 600, 700, 750, 800, and 900 °C (T_0 values). The combustion reactions took place spontaneously upon complete evaporation of the solvents and produced voluminous white powders, which were removed from the furnace after 2 min, and allowed to cool rapidly to room temperature. The produced specimens were coded according to T_0 and synthesis fuel as U400–U900 and S400–S900, respectively. Adiabatic temperature values (T_{ad}) for each synthesis reaction were calculated based on the molar enthalpy values of each raw material from HSC 6 Chemistry software [24] and Lange's Handbook Of Chemistry (Eq. (E4S), Appendix Section) [25].

2.2. Characterization

The presence of crystalline phases in the glass powders was analyzed by XRD measurements using a GNR's X-Ray diffractometer, employing $\text{Cu-K}\alpha$ radiation ($\lambda = 1.54\text{ \AA}$) at 40 kV and 30 mA. The 2θ range of $20\text{--}80^\circ$ was probed at room temperature with step-scanning of 0.01° and an integration time of 2s. Infrared spectra were recorded by Fourier transform infrared spectroscopy (FTIR) in the range of $400\text{--}4000\text{ cm}^{-1}$ on a Thermo Nicolet, AVATAR 370, USA spectrometer on pellets with fixed amounts of sample and KBr. Raman spectroscopy was performed on a confocal Raman spectroscopy system (Jobin–Yvon Horiba (LABRAM-HR) spectrometer) in the range of $400\text{--}1600\text{ cm}^{-1}$. The selected excitation wavelengths were 532 nm and 780 nm. The data were first normalized at a wavelength of 780 nm and then deconvoluted with several mixed Gaussian-Lorentzian signal components. The peak positions were optimized by the least-squares fitting leveraging algorithm (Levenberg-Marquardt). The microstructure of the glasses was characterized by using FESEM microscopy, performed by MIRA3, TESCAN microscope using an accelerating voltage of 15 kV. The samples were sputter-coated with gold for 180s. Thermogravimetry (TG) and differential thermal analysis (DTA) of the glasses and raw materials were carried out with a 6000 PerkinElmer simultaneous thermal analyzer (STA) under an inert atmosphere at temperatures ranging from 50 to 1100 °C with heating rates of 10 and 15 °C/min, respectively.

2.3. NMR studies

Solid-state NMR experiments were carried out on a Bruker Avance 500 MHz spectrometer operating at a magnetic flux density of 11.74 T. ^{11}B , ^{23}Na , and ^{31}P direct polarization magic-angle spinning (MAS)-NMR experiments and ^{11}B EASY MAS-NMR experiments were conducted using a commercial 4 mm H/X/Y DVT probe operating at a MAS frequency of 10 kHz and using 4 mm o.d. (3 mm i.d.) ZrO_2 rotors with Vespel caps. ^{11}B , ^{23}Na , and ^{31}P chemical shifts are reported for $\text{BF}_3 \cdot \text{Et}_2\text{O}$ (0 ppm), NaCl (0 ppm, 1 M aq. solution), and concentrated H_3PO_4 (0 ppm), respectively. For S750 and U900, additional ^{31}P spectra were obtained on a Bruker Avance 200 MHz spectrometer with a longer acquisition time (S750: 5200 scans, U900: 5700 scans, corresponding to 3.6 and 4 days of acquisition, respectively) and $\nu_{\text{MAS}} = 8$ kHz under otherwise identical acquisition parameters. For the ^{11}B and ^{23}Na MAS-NMR spectra, small-flip angle excitation pulses and long relaxation delays of 32 s were chosen to ensure quantitative NMR spectra (see Table 2). The ^{11}B , ^{23}Na , and ^{31}P spectra were deconvoluted by fitting adequate line-shape models implemented in the ssNake software [26] to the data deploying the Powell minimization method: quadrupolar CT line-shapes considering the effects of the second-order quadrupolar interaction for ^{11}B , a Cjzek distribution [27,28] of quadrupolar parameters for all broad ^{23}Na components, and mixed Gauss-Lorentzian components for all ^{31}P and narrow ^{23}Na components.

^{11}B z-filtered triple quantum MAS (3QMAS) experiments with 24-step nested phase-cycling were recorded using the States-TPPI procedure [29] in a 2.5 mm H/X/Y DVT probe operating at a MAS frequency of 20 kHz and 2.5 mm o.d. (1.7 mm i.d.) ZrO_2 rotors with Vespel caps. Excitation, reconversion, and z-Filter pulses were optimized to yield maximum signal intensity of the B^3 signal component. The delay between the first two rf-pulses was incremented in steps of $t_1 = 1/\nu_{\text{MAS}}$, corresponding to a spectral width of $\nu_{\text{MAS}} = 20$ kHz in the indirect dimension. Each 3QMAS spectrum was recorded in 12 h and is shown after appropriate Fourier and shearing transformations using the parameters indicated in Table 2. For the sake of time, the acquisition was limited to 120 increments, which may lead to minor spectral distortions due to incomplete decay of 3Q coherence of the crystalline B^3 and four-coordinated B^4 sites.

Quadrupolar product (P_Q) values were obtained from the center of gravity of the signals in the anisotropic (δ_{D2}) and isotropic (δ_{D1}) projections of the sheared 3QMAS spectra as follows:

Table 2

Larmor frequency ν_0 , NMR experiment, nutation frequency ν_1 , pulse length t_p , flip angle θ (w.r.t. single quantum excitation), MAS frequency ν_{MAS} , recycle-delay d_1 , and some recorded transients ns, employed in the NMR experiments.^a For the 3QMAS experiment, the pulse lengths of the excitation, refocusing, and z-Filter pulses are given, rather than t_p .^b Measurements at 4.7 T.

Nucleus	ν_0 /MHz	NMR experiment	ν_1 /kHz	t_p /μs	θ /rad	ν_{MAS} /kHz	d_1 /s	ns
^{11}B	160.46	EASY	111	0.3	$\pi/18$	10	32	132
		z-filtered 3QMAS	222	2.4, 0.9, 21.0 ^a	–	20	6	48 · 128
^{23}Na	132.30	MAS	50	0.3	$\pi/33$	10	2	824 to 14200
^{31}P	202.47	MAS	56	4.5	$\pi/2$	10	480	4 (U900), 700 to 800 (all others)
							60	5280 (S750) 5700 (U900)
	81.04 ^b	MAS	33	7.5	$\pi/2$	8	60	5280 (S750) 5700 (U900)

$$\delta_{\text{iso}} = \frac{17\delta_{D1} + 10\delta_{D2}}{27} \quad (1)$$

and

$$P_Q = \sqrt{z \cdot 10^{-6} \nu_0^2 (\delta_{D1} - \delta_{D2})} = C_Q \sqrt{1 + \frac{\eta^2}{3}} \quad (2)$$

Where $z = 680/27$ for $I = 3/2$ and ν_0 , C_Q , and η are the transmitter offset frequency, the quadrupolar coupling constant, and the asymmetry factor of the electric field gradient (EFG), respectively [30].

3. Results and discussion

3.1. X-ray powder diffraction

The XRD results of the synthesized glass powders in the presence of urea and sucrose are shown in Figs. 1 and 2, respectively. The diffractograms of all samples, except for U900 and S900 samples, indicate the presence of two broad peaks at 2θ angles of 28 and 44°, which are representative of variable d-spacings found in glasses [8]. In the U400 sample, two additional broad peaks with low intensity can be observed at

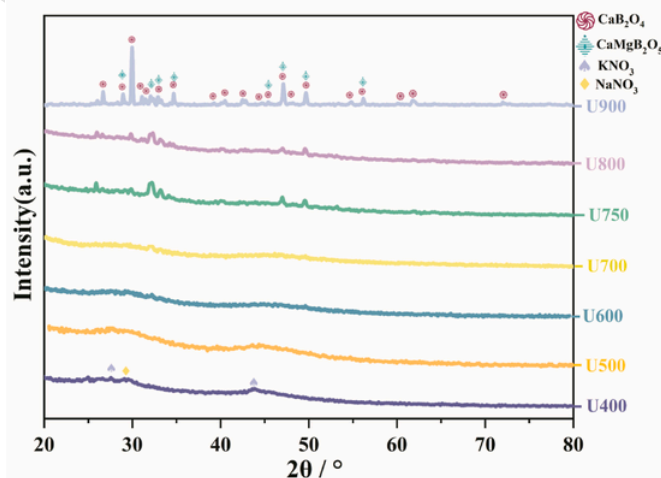


Fig. 1. Powder x-ray diffraction patterns of the synthesized glass powders in the presence of urea as the fuel.

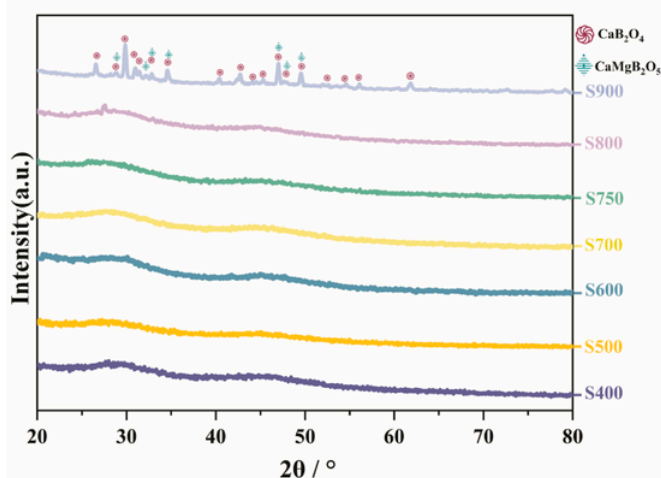


Fig. 2. Powder x-ray diffraction patterns of the synthesized glass powders in the presence of sucrose as the fuel.

27° (ICDD 96-210-4623) and 29° (ICDD 96-900-7561), possibly existing due to the minor amounts of residual KNO_3 and NaNO_3 precursors, respectively [20]. The absence of the peaks mentioned above in the S400 sample may be explained by the overall lower volume of released gas using sucrose as the fuel than released gas using urea (chemical reactions of (E1S) and (E2S)) and the possible decrease in the heat losses due to a less turbulent combustion reaction [31]. When urea was used as the fuel at T_0 values above 750 °C, new XRD peaks could be observed, attributable to the crystalline phases of CaB_2O_4 (ICDD 96-101-0438, $2\theta = 29.870$) and CaMgB_2O_5 (ICDD 96-901-0723, $2\theta = 32.104$). It has been shown that calcium metaborate and trivalent terbium-doped CaMgB_2O_5 may form by the SCS method using urea as the fuel at T_0 values of 500 and 600 °C, respectively [32,33].

3.2. FESEM

FESEM images of the synthesized glass powders in the presence of urea and sucrose as fuels are displayed in Figs. 3 and 4, respectively. All samples exhibit smooth surfaces with many different-sized pores. The latter is most likely the result of the gas release during the synthesis process [34]. Indication for some crystalline material can be found in the microstructure of the U900 and S900 samples, indicated by arrows in Figs. 3c and 4c. In light of the XRD patterns, these morphologies should be related to CaB_2O_4 or CaMgB_2O_5 phases [32,33].

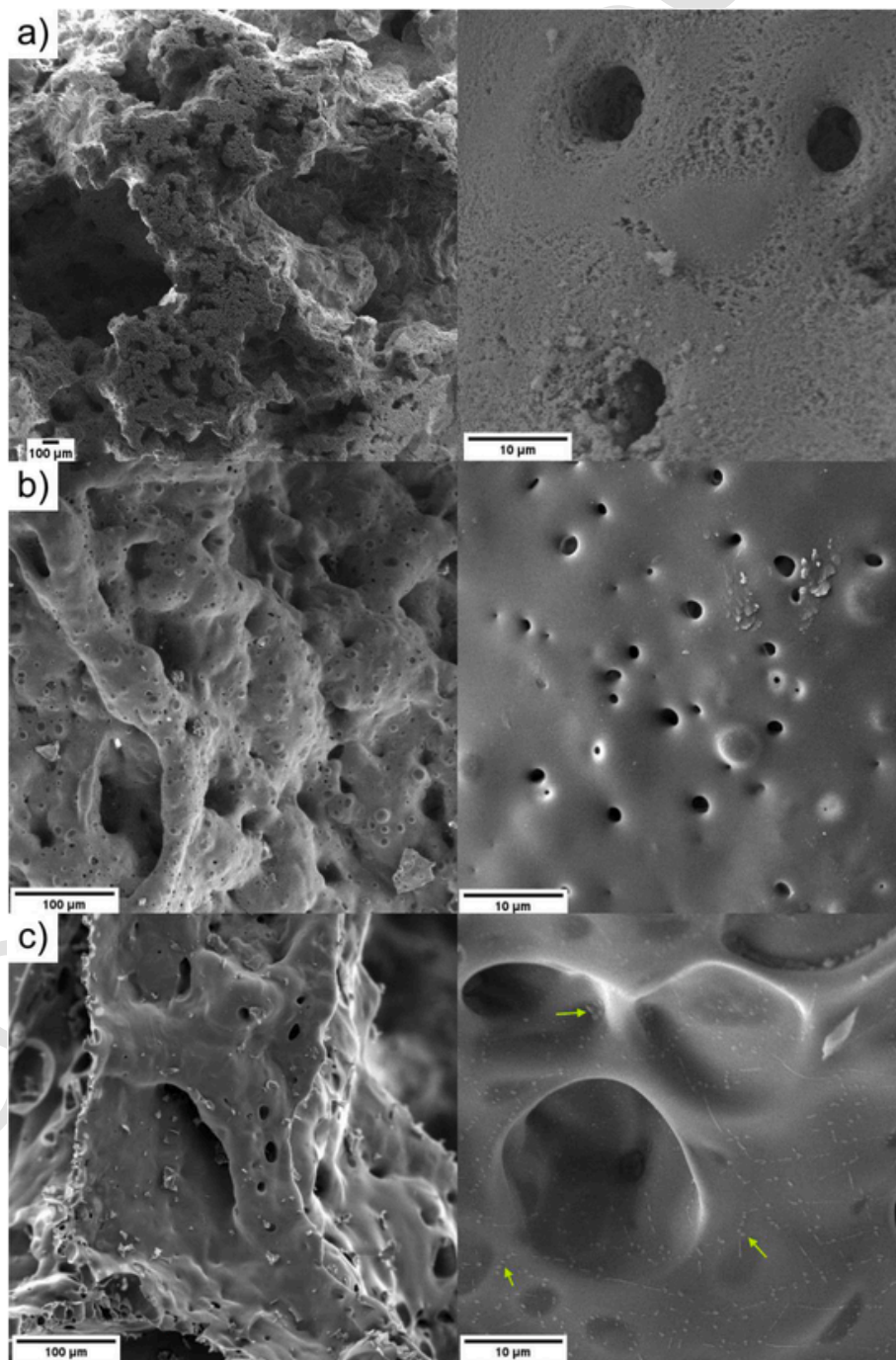


Fig. 3. FESEM images of a) U400, b) U600, and c) U900 samples.

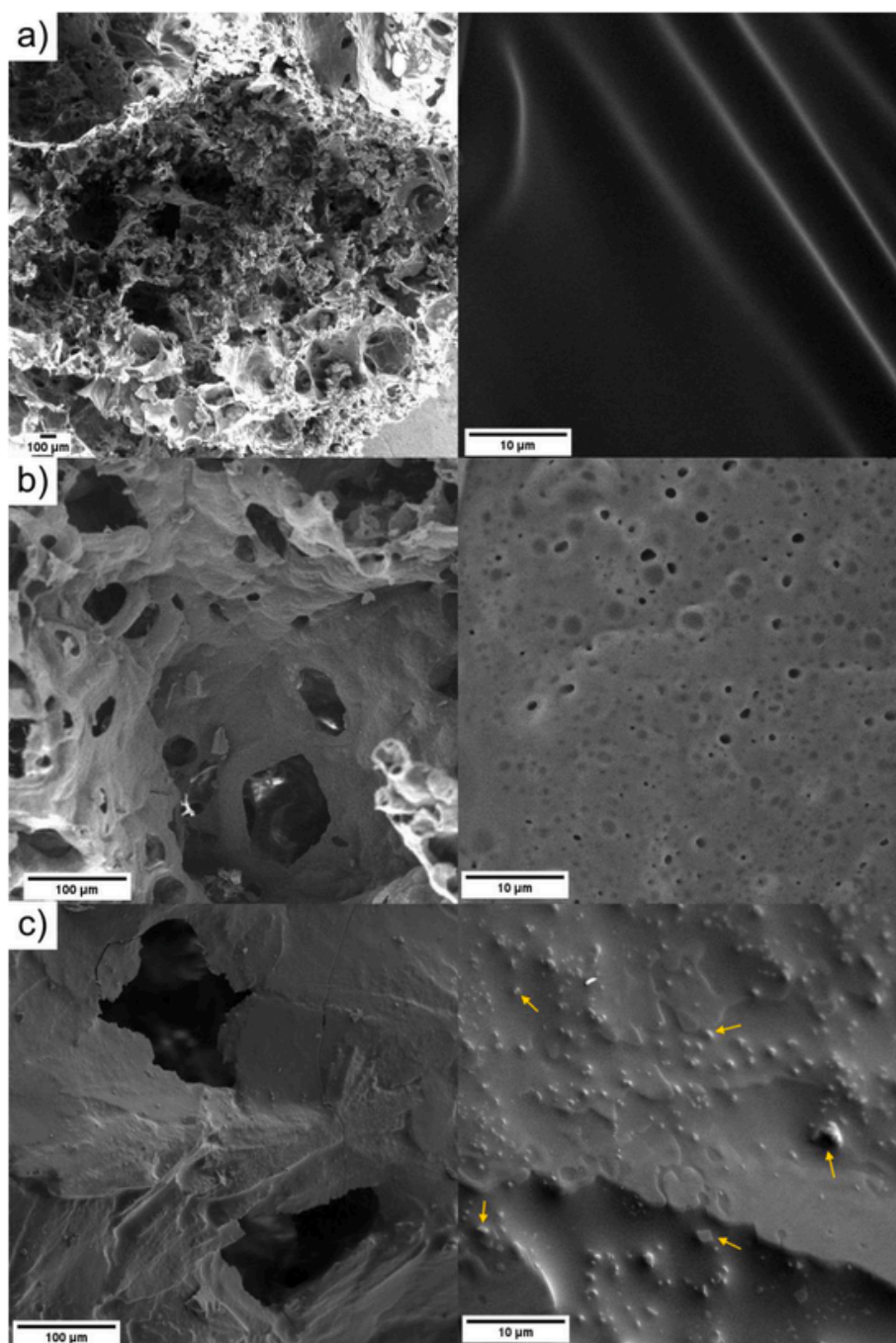


Fig. 4. FESEM images of a) S400, c) S600, and c) S900 samples.

3.3. DTA-TG

It is generally accepted that the phase formation and microstructure of materials produced by the SCS method depend on the interplay between reaction rates, combustion temperatures, and the rates of gas release in the reaction. Unfortunately, the SCS method is quite complex, and the number of studies on its reaction kinetics is limited. For the sake of discussing the observed properties of the materials under study, we used adiabatic temperature calculations as a proxy for the actual combustion temperatures. It should be noted that the informative value of adiabatic temperatures is limited, given that the equilibrium products for the studied systems are assumed to be the intended 1393-B3 composition, while the actual final products are unknown.

DTA-TG curves of S400, S500, and S700 are shown in Fig. 5, and the characteristic temperatures T_0 , glass transition temperatures (T_g), and adiabatic temperatures T_{ad} are listed in Table 3. As expected from equation E4S (Appendix Section), increasing furnace temperatures T_0 result in higher theoretical T_{ad} values [20,35]. Similarly, the DTA curves show that T_g values increase with T_0 , which implies some effect of the initial furnace temperature on the structure of the glasses. Often, increased glass transition temperatures are observed in borate glasses whenever the amount of connected $[BO_3]$ structural units increases, which goes hand in hand with an improvement in the chemical stability of the glasses [36,37]. Beyond $T_{ad} = 1047$ °C for Urea and 913 °C for sucrose, the DTA curves show the partial crystallization of the samples, which mask the glass transition events rendering the determination of T_g impossible (DTA data not shown). This difference of about 130 °C be-

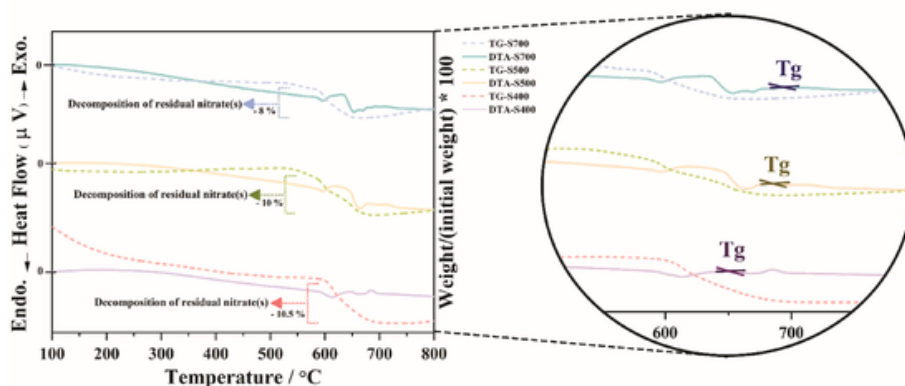


Fig. 5. DTA-TG curves of the as-synthesized S400, S500, and S700 samples.

Table 3

Initial temperature of the combustion area (T_0), glass transition temperature (T_g), and adiabatic temperature (T_{ad}) of samples.

Sample X = (U, S)	$T_0/^\circ\text{C}$	$T_g/^\circ\text{C}$	$T_{ad}/^\circ\text{C}$	
			Urea	Sucrose
X400	400	652 ± 3	668	576
X500	500	674 ± 3	795	673
X600	600	683 ± 3	933	768
X700	700	687 ± 3	1047	865
X750	750	Containing crystalline phases	1140	913
X800	800	Containing crystalline phases	1214	961
X900	900	Containing crystalline phases	1376	1057

tween the apparent onset temperatures is expected from the higher gas release of the urea system leading to higher heat losses.

The TG curves of all samples indicate weight losses of $\sim 10.5\%$, 10% , and 8% for S400, S500, and S700, respectively, in the temperature range of ~ 550 – 680 °C. The origins of these weight losses may lie in unreacted nitrate precursors, which are left over after the turbulent combustion reaction. In order to test this hypothesis, DTA-TG measurements were performed on the precursors, namely on NaNO_3 , a mixture of $\text{NaNO}_3 + \text{KNO}_3$, a mixture of all nitrates of the 1393-B3 composition (NaNO_3 , KNO_3 , $\text{Ca}(\text{NO}_3)_2$, $\text{Mg}(\text{NO}_3)_2$) and a mixture of all reagents used in the synthesis of the 1393-B3 glass powders (see Section S3 of the Appendix Section for more details). In summary, the results show that the decomposition process for pure NaNO_3 and a mixture of $\text{NaNO}_3 + \text{KNO}_3$ starts at about 700 °C and proceeds steadily. The same behavior can be observed for the complex mixtures; however, the onset of the decomposition is found between 630 and 750 °C. These observations contrast the onset of the weight losses measured for the synthesized samples near 600 °C. Careful inspection of the data reveals that the weight loss in S500 and S700 coincides with endothermic events observed in the DTA curves, in even multiple steps between about 550 – 600 °C and 600 – 650 °C. However, considering the absence of significant XRD peaks of nitrate compounds in the mentioned samples (Fig. 2, given that the detection limit of about 5%), the weight losses can only be partially explained by the residual precursors and suggest a more complex decomposition process occurs, such as the possible volatilization of the surface boron species [38].

3.4. FTIR

Figs. 6 and 7 show the FTIR spectra of the synthesized glasses using urea and sucrose as fuels, respectively. Since the main spectral fea-

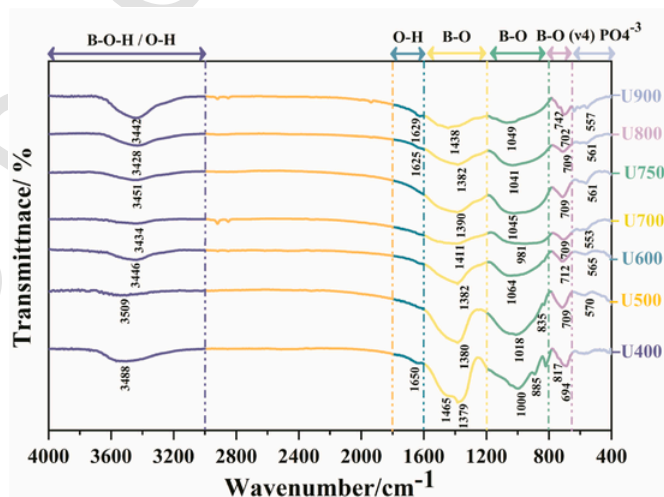


Fig. 6. FTIR spectrum of the synthesized glass powders in the presence of urea as the fuel.

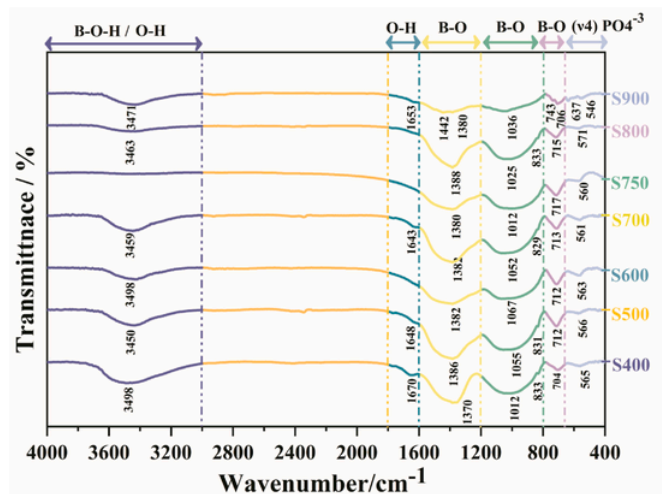


Fig. 7. FTIR spectrum of the synthesized glass powders in the presence of sucrose as the fuel.

tures of all samples are independent of the fuel type, the following results will be discussed jointly. The characteristic bands of all samples are summarized in Table 4. The broad band observed in the region of 3400 – 3500 cm^{-1} indicates the presence of O–H groups stemming

Table 4
Band assignments for IR spectra of the synthesized glass powders.

FTIR wavenumbers (cm ⁻¹)	Assignment	Ref
3400–3500, 1600	B–O–H groups and surface adsorbed H ₂ O	[44]
1200–1600	B–O bond's stretching vibrations in trigonal BO ₃ groups	[44]
800–1200	B–O stretching vibrations in tetrahedral BO ₄ groups	[44]
600–800	B–O–B bending vibrations in BO ₃ and BO ₄ groups	[44]
400–600	PO ₄ ⁻³ groups	[44]
830, 1380, 1650	NO ₃ ⁻ groups	[42]

from physically adsorbed water [39–41] or BOH units or which are known to be prone to water absorption [42]. Similarly, the samples show a somewhat less defined absorption band at about 1600–1700 cm⁻¹, which can also be attributed to the O–H bond of physically adsorbed water [40]. Signals between 1200 and 1600 cm⁻¹ are characteristic of B–O stretching modes in trigonal BO₃ groups. Their intensity in the spectra decreases for T_0 values above 700 °C and 600 °C for urea and sucrose fuels, respectively. Note that the decrease is less pronounced in the latter case (i.e., using urea as fuel). Moreover, a further increase in the T_0 values does not seem to change the absorption band's strength systematically in either case.

The adjacent absorption region between 800 and 1200 cm⁻¹ can be assigned to the B–O stretching vibrations of tetrahedral BO₄ groups. No clear trend between the intensity of the mentioned band with the T_0 values can be observed. However, it should be noted that for the U400 sample, many narrow absorption signals are found throughout the discussed regions, indicating the presence of boron in a crystalline structural environment [43]. The bands at 600 to 800 cm⁻¹ stem from B–O–B bending vibrations of both BO₃ and BO₄ groups [44]. Both U900 and S900 samples exhibit narrow signals in this region, confirming the formation of the CaMgB₂O₅ and CaB₂O₄ phases detected by XRD.

Lastly, FTIR bands at wavenumbers below 600 cm⁻¹ are evidence of the internal modes of PO₄⁻³ groups [44,45], which have relatively poor resolution, owing to the overall low P₂O₅ content of the samples. While this evaluation of the FTIR spectra validates the expected bands for a borate glass, the work of Li et al. [46] pointed out that BOH structural groups can trap nitrate groups released during the combustion synthesis process. The characteristic bands of nitrate groups typically could be found at wavenumbers near ~830 cm⁻¹, ~1380 cm⁻¹, and ~1650 cm⁻¹ [10,47,48]. In the current research, however, only an absorption band near 1389 cm⁻¹ was observed.

3.5. Raman

Figs. 8–11 show the Raman spectra of the synthesized glass powders (i.e., U400, U700, S400, and S750) using urea and sucrose as fuels. Boron-oxide-containing glasses are expected to have a fraction of BO₃ and BO₄ structural units depending on the network modifier content [13]. BO₃ and BO₄ structural units can form superstructural units, such as boroxol ring(s), diborate, triborate, tetraborate, metaborate, and pentaborate groups [49]. Table 5 summarizes the observed B–O vibrational bands detected in the synthesized samples and their attribution to the related superstructural units. In the Raman spectra of the U400 (cf. Fig. 8), two peaks at ~725 cm⁻¹ and ~1260 cm⁻¹ correspond to the B–O band in the metaborate chains and pyro-borate groups, respectively [50]. Moreover, the intense band at 1050 cm⁻¹ may indicate the presence of some NO₃⁻ groups [47]. A comparison of the Raman spectra of U700 with U400 demonstrates that with increasing the T_0 values, two new peaks appear at ~950 and ~1350 cm⁻¹, corresponding to ortho-borate, and metaborate groups, respectively [50]. It should be noted that the peaks at ~950 and ~1050 cm⁻¹ can

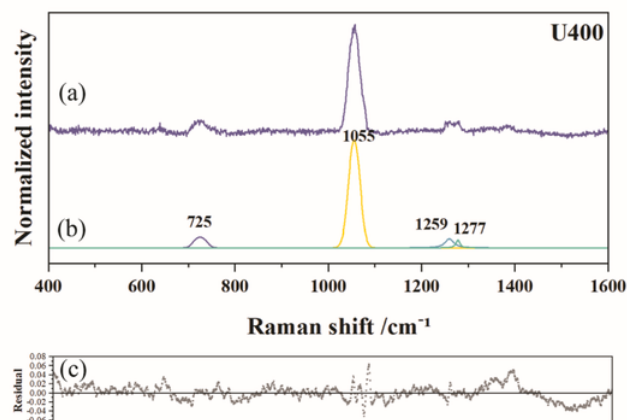


Fig. 8. a) normalized, b) deconvoluted, c) associated residual of the Raman spectra of the synthesized glass powders in the presence of urea as the fuel at 400 °C (excitation wavelength of 780 nm).

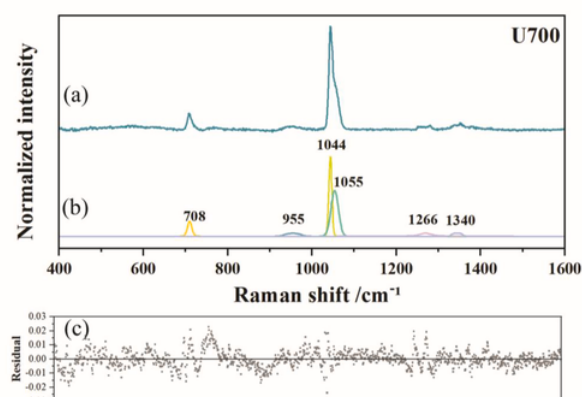


Fig. 9. a) normalized, b) deconvoluted, c) associated residual of the Raman spectra of the synthesized glass powders in the presence of urea as the fuel at 700 °C (excitation wavelength of 780 nm).

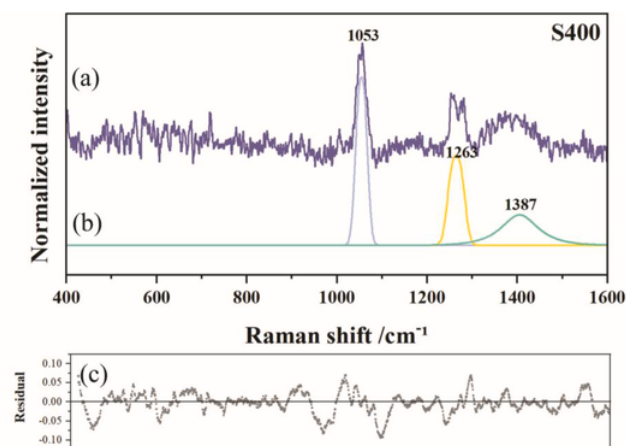


Fig. 10. a) normalized, b) deconvoluted, c) associated residual of the Raman spectra of the synthesized glass powders in the presence of sucrose as the fuel at 400 °C (excitation wavelength of 780 nm).

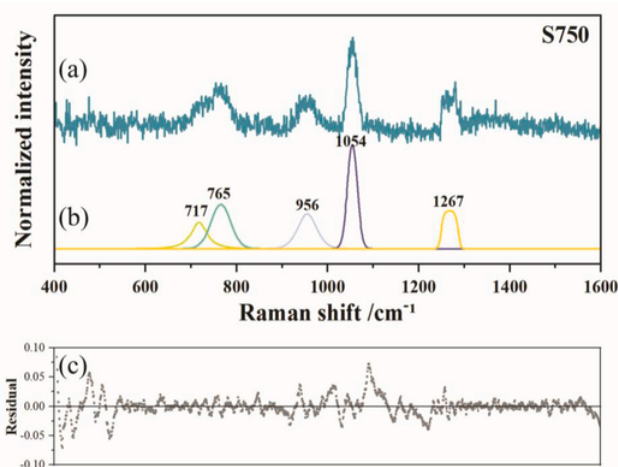


Fig. 11. a) normalized, b) deconvoluted, c) associated residual of the Raman spectra of the synthesized glass powders in the presence of sucrose as the fuel at 750 °C (excitation wavelength of 780 nm).

Table 5

Assignment of the prominent Raman bands in the spectra of the synthesized glass powders.

Raman shift (cm ⁻¹)	Assignment	Ref
465–500	isolated diborate groups	[44]
433	symmetric bending vibrations of P–O bonds in Q ¹ tetrahedrons	[47]
535	diborate units	[44]
558	symmetric bending vibrations of P–O bonds in Q ¹ tetrahedrons	[47]
600–650	symmetric breathing vibrations of metaborate rings	[44]
602	bending vibrations of P–O–P in Q ²	[47]
700–735	symmetric breathing vibrations of metaborate chains	[44]
714	symmetric stretching of P–O–P linkages in Q ² and Q ¹ structural units	[47]
740–775	symmetric breathing vibrations of six-membered rings with one BO ₄ ⁻ tetrahedra units	[44]
765	B–O–B bending mode	[44]
835–840	pyroborate vibrations	[44]
875–1000	ortho-borate groups	[44]
945	symmetric stretching vibrations of P–O bond in Q ⁰ tetrahedrons	[47]
1000–1110	diborate groups	[44]
1030	symmetric stretching vibrations of P–O bond in Q ¹ tetrahedrons	[47]
1050	NO ₃ ⁻	[42]
1216–1260	pyro-borate groups	[44]
1290	symmetric stretching vibrations of P–O bonds in Q ² tetrahedrons	[47]
1300–1600	B–O-stretching in metaborate rings and chains	[44]

also be characteristic of the P–O band in Q⁰P and Q¹P units, respectively [51,52]. The Raman spectrum of S400, see Fig. 10, reveals bands at ~1260 and ~1380 cm⁻¹ that can be attributed to the B–O vibration in pyroborate and metaborate groups, respectively [50]. Again, the band located at around ~1050 cm⁻¹ may be related to NO₃⁻ groups in this sample [47], while the bands at ~1050 and ~1260 cm⁻¹ can also be associated with P–O in Q¹P, and Q²P units, respectively [51,52]. As shown in the Raman spectrum of S750 in Fig. 11, increasing T_0 to 750 °C results in new peaks at ~715, ~770, ~950, and ~1260 cm⁻¹. The peak at ~715 cm⁻¹ could be related to the B–O stretching in metaborate chains [50], while the band at ~770 cm⁻¹ could be due to the B–O vibrational mode of six-membered rings involving one BO₄⁻ tetrahedra unit [50]. Furthermore, the bands at

~950 and ~1260 cm⁻¹ evidence ortho- and pyroborate groups, respectively [50]. The peaks at ~715 and ~950 cm⁻¹ can also be associated with P–O–P linkages in Q²P and Q¹P structural units and the P–O band in Q⁰P units, respectively [51,52].

As seen from Figs. 8–11, the type of reaction fuel and the synthesis temperature appear to affect the short to intermediate range-order of the network former units in the produced glass powders.

3.6. NMR

3.6.1. ¹¹B MAS NMR

Fig. 12 shows the effect of varying T_0 values on the ¹¹B EASY MAS NMR spectra of the 1393-B3 glass powders under study. All spectra exhibit characteristic line-shape features attributable to at least two different borate environments: (1) a relatively narrow Gaussian resonance line (400–450 Hz FWHM) centered around one ppm that indicates four-coordinated B⁴ units in which the ¹¹B nuclei are subjected to relatively weak EFGs due to the high symmetry of their coordination polyhedra, and (2) a broad, two-peaked component attributable to trigonally coordinated B³ units centered at about 12 ppm. The observed B³ units can further be differentiated as Tⁿ units, whereas 0 ≤ n ≤ 3 indicates the number of bridging oxygen atoms [53–55]. T³ units are usually present in the ring structures of the borate network and will be denoted as B_n³. Similarly, T², T¹, and T⁰ species correspond to the anionic metaborate, pyroborate, and orthoborate units, respectively, and will be jointly referred to as B_a³. By increasing the T_0 values, changes can be observed in the ¹¹B NMR spectra. For both synthesis fuels, an increase in the B³ fractional areas becomes apparent, accompanied by subtle line-shape changes attributable to the formation of additional B³ species.

In order to quantitatively describe these changes and to distinguish between the overlapping signals of multiple B³ and B⁴ species, it is necessary to arrive at satisfactory line-shape deconvolutions. Thus, 3QMAS NMR experiments were conducted to increase the spectral resolution, and the obtained spectra are presented in Fig. 14 and S5 (in the Appendix Section). Upon inspection of the vertical projections of the 3QMAS spectra, multiple B³ species can be identified for U900 and S900 samples, while differentiation of multiple B⁴ species is only possible for the U400 sample. Isotropic chemical shifts (δ_{iso}) and P_Q values of B³ and B⁴ signals are calculated from the second-order quadrupolar shift according to Equations (1) and (2) and are presented in Table 6.

For U900 and S900, an additional narrow signal component along the isotropic (F1) dimension is observable near 22 ppm, indicating a much narrower distribution of local EFGs found in crystalline phases (see Table 7). This result suggests the partial crystallization of the borate network at T_0 values above about 700 °C. Furthermore, these signals' lower second-order quadrupolar shift acknowledges a smaller quadrupolar coupling constant (C_Q) than the “glassy” B³ signal component.

In addition, the isotropic broadening of B³ and B⁴ components in the spectrum of the U400 sample is much lower than in the other samples. Note that due to the narrow contour profiles and vertical projection of the 3QMAS NMR spectra, both signal components (i.e., B³ and B⁴) are upshifted by about one ppm. A higher ordering of the boron network is explainable by residual precursor material leftover principally at lower T_0 values. Although a complete separation of both B³ components is not achieved at the given spectral resolution, it was possible to arrive at satisfactory and robust line-shape deconvolutions of the MAS NMR spectra, as shown in Fig. 13 and Fig. S4, based on the physical constraints given by position, quadrupolar product, and line-shape features. The corresponding NMR parameters and the fractional areas of the three- and four-coordinate boron species are listed in Table 6.

Charge balance requirements enforce that for the given per-boric glass composition (network modifier/B₂O₃ ratio $R \approx 0.8$), anionic B³ species have to be present in all materials since the sum of anions im-

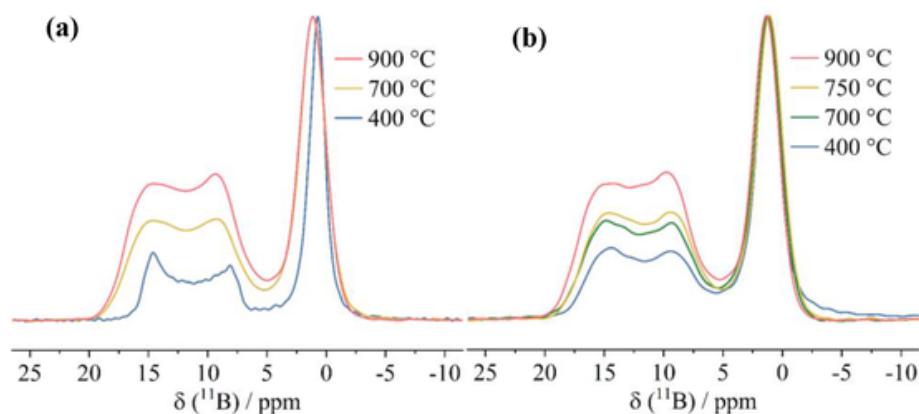


Fig. 12. Experimental ^{11}B EASY MAS NMR spectra of the synthesized glass powders at varying T_0 values (indicated by the legend) using (a) urea and (b) sucrose as fuels. The intensities of all signals are normalized to the most intense signal stemming from B4.

Table 6

Fit parameters obtained from deconvolution of the ^{11}B spectra shown in Fig. 13 and S4. For B4, only the P_Q value is reported based on the SOQS observed in 3QMAS measurements. δ_{SOQS} is the second order quadrupolar shift obtained from the respective 3QMAS spectra. δ_{SOQS} corresponds to the isotropic dimension's shift (center of gravity).

Sample	^{11}B species	$\delta_{\text{iso}} / \text{ppm}$	$C_Q (P_Q) / \text{MHz}$	η_Q	$\delta_{\text{SOQS}} / \text{ppm}$	$f / \%$	lb/Hz
U400	B_1^4	1.1	(0.62)	0.0	1.8	0.53	294
	B_2^4	2.2	(0.72)	0.0	2.4	0.05	448
	B_n^3	17.3	2.51	0.0	21.7	0.39	479
	B_a^3	16.6	2.47	0.1		0.05	193
U700	B^4	1.3	(0.48)	0.0	2.2	0.45	447
	B_n^3	18.6	2.63	0.0	23.5	0.39	471
	B_a^3	17.0	2.53	0.5		0.16	465
U900	B^4	1.3	(0.42)	0.0	2.2	0.35	448
	B_n^3	18.7	2.62	0.0	23.0	0.43	512
	B_a^3	17.0	2.57	0.5	21.9	0.22	481
S400	B^4	1.5	(0.50)	0.0	2.2	0.57	432
	B_n^3	18.2	2.58	0.0	22.9	0.32	470
	B_a^3	17.3	2.50	0.5		0.11	464
S700	B^4	1.3	(0.45)	0.0	2.1	0.46	437
	B_n^3	18.6	2.63	0.0	23.1	0.43	473
	B_a^3	17.0	2.53	0.5		0.11	337
S750	B^4	1.3	(0.48)	0.0	2.1	0.44	447
	B_n^3	18.6	2.63	0.0	23.3	0.42	471
	B_a^3	17.0	2.53	0.5		0.15	465
S900	B^4	1.5	(0.42)	0.0	2.3	0.35	431
	B_n^3	18.9	2.62	0.0	23.5	0.44	517
	B_a^3	17.0	2.57	0.5	22.0	0.21	514

plied from the presence of tetragonally coordinated borate and phosphate species is insufficient to fully compensate cationic Mg^{2+} , Ca^{2+} , K^+ , and Na^+ charges. Therefore, an additional line shape component is included in the total deconvolution (see Table 6), corresponding to an anionic borate species (B_a^3). The modeled δ_{iso} , C_Q , and η_Q values of the anionic B^3 component complied with values reported for T^2 species in $\text{CaO-B}_2\text{O}_3$ glass that consists of anionic polyborate $[\text{BO}_2]_{\infty}^-$ chains. It should be noted that due to the complexity of the glass system, non-differentiable T^3 , T^2 , and T^1 environments may be present here, especially concerning the similar line-shape characteristics of T^2 and species [53–55].

The B^3 species of all spectra feature isotropic chemical shifts of $\delta_{\text{iso}} = 18.6 \pm 0.5$ ppm, a characteristic quadrupolar coupling constant of $C_Q = 2.6$ MHz, and a low EFG asymmetry parameter of $\eta_Q \sim 0.0$ – 0.1 indicating the presence of mainly neutral metaborate T^3 units [53,54,56]

Table 7

Fit parameters obtained from the ^{31}P MAS NMR spectra are shown in Fig. 16. The deconvolutions of the ^{31}P MAS NMR spectra are shown in Fig. S6.

Sample	^{31}P species	$\delta_{\text{iso}} / \text{ppm}$	f/%	lb/Hz
U400	P_{g1}	-2.0	77	1986
	P_{g2}	2.5	23	1120
U700	P_g	4.8	37	1494
	P_g	1.1	63	1621
U900	P_c	4.1	72	280
	P_c	1.5	5	161
	P_g	-0.8	23	822
S400	P_c	1.6	16	375
	P_g	-0.5	84	2116
S700	P_c	1.6	10	710
S750	P_g	-0.1	90	2610
S900	P_{c1}	3.9	60	401
	P_{c2}	1.8	34	369
	P_{c3}	1.0	5	129

Table 8

Fit parameters obtained from the ^{23}Na MAS NMR spectra shown in Fig. 17. The deconvolutions of the ^{23}Na MAS NMR spectra are shown in Fig. S7.

Sample	^{23}Na species	$\delta_{\text{iso}} / \text{ppm}$	σ / MHz	f/%	lb/Hz
U400	Na_g	-2.6	0.34	35	1272
	Na_{c3}	-4.6	0 ^a	65	215
U700	Na_g	1.9	1.57	70	1554
	Na_{c1}	-12.6	0 ^a	11	342
	Na_{c2}	-7.4	0 ^a	19	377
U900	Na_g	-3.4	0.82	100	2817
S400	Na_g	-7.2	0.46	71	1335
	Na_{c2}	-7.5	0 ^a	29	225
	Na_g	-2.9	0.92	74	2055
S700	Na_{c1}	-12.6	0 ^a	10	223
	Na_{c2}	-7.5	0 ^a	16	749
	Na_g	-6.2	0.87	84	2210
S750	Na_{c1}	-12.6	0 ^a	16	207
	Na_g	-1.4	1.28	96	2442
S900	Na_{c2}	-7.5	0 ^a	4	503

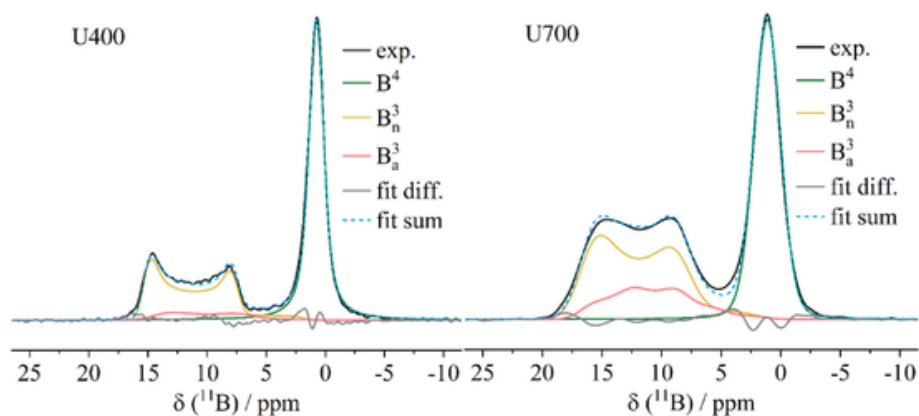


Fig. 13. Exemplary line-shape deconvolutions of the experimental ^{11}B EASY MAS NMR spectra of U400 and U700 samples. The line-shape components assumed for each fit are determined from 3QMAS experiments (see Fig. 14 and S5), Raman results, and charge balance considerations. Interaction parameters and intensities are determined through least-squares fitting respecting physical constraints of possible NMR parameters for trigonally planar coordinated ^{11}B species.

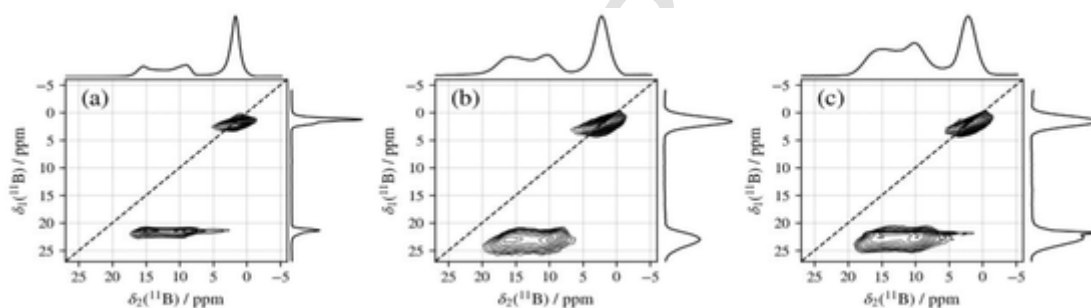


Fig. 14. ^{11}B 3QMAS NMR spectra of the glass samples synthesized with urea at 400, 700, and 900 °C. The crystalline components in the spectra of S400 and S900 samples are visible as narrow high-field ridges in the isotropic (vertical or δ_1) dimension absent in the S700 sample.

(denoted in the following as B_n^3). The found upshift concerning the chemical shift of T^3 units present in pure B_2O_3 glass [53] shows that the second-coordination sphere around boron is composed of dominantly B^3 and B^4 units (i.e., B–O–B linkages are formed) [54]. The initially observed monotonous increase in B^3 fractional area following increasing the T_0 values can be quantitatively described in terms of an N_4 value reduction [56] from about 55% at $T_0 = 400$ °C to 34% at $T_0 = 750$ °C. Surprisingly, these values differ significantly from the N_4 value of 40% reported for a 1393-B3 glass produced by melt quenching at 1050 °C (see Fig. 15) [57]. The observed N_4 values are lower by about 1–3% when sucrose is used as fuel.

In the present case, the dependence of the fictive temperature on the synthesis conditions is striking. It is known from thermal treatment studies on melt-quenched borate glasses that N_4 values decrease with higher cooling rates [58,59], as the present $B^4 \leftrightarrow B^3$ equilibrium shifts towards the right side of the equation at higher fictional temperatures due to the breaking of B–O–B bounds in diborate rings. Ongoing annealing experiments on the U400, S400, and S750 samples (data not shown here) and consecutive cooling on a metal plate (quench rates of 100–1000 K/min) indicate a much lower variational range for N_4 after quenching, regardless of the used sample. This result verifies that the SCS method can achieve a more extensive range of fictive temperatures than is accessible by melt quenching or annealing.

3.6.2. ^{31}P MAS NMR

The ^{31}P MAS NMR spectra of the studied samples are shown in Fig. 16. Measurements using different recycle delays of 60 s and 720 s show no changes regarding spectral features and line widths. This result suggests that the measurements are quantitative under the employed conditions. Tentative line-shape deconvolutions were done using one to three Gaussian components, as shown in Fig. S6. For T_0 values up to

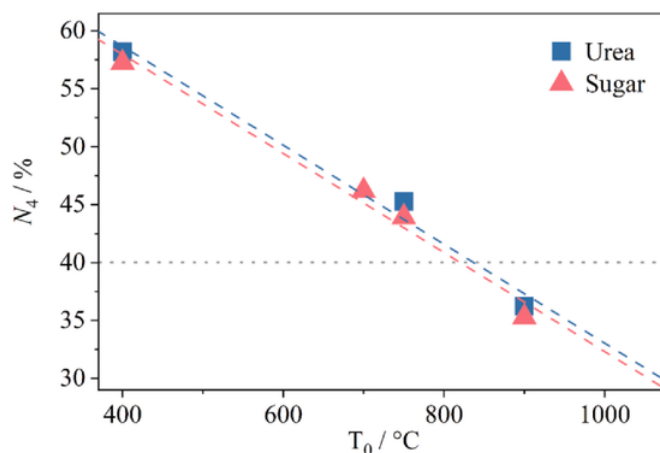


Fig. 15. N_4 values of 1393-B3 glasses against different T_0 values. The dashed lines are extrapolations of the N_4 values to other T_0 values. The horizontal dotted line indicates the reported N_4 values for a melt-quenched 1393-B3 glass [56].

600 °C, all spectra are characterized by asymmetric line shapes with limited resolution and isotropic chemical shifts ranging between -0.2 ppm and 4.1 ppm. This chemical shift range is characteristic of orthophosphate ($\text{Q}^0 / \text{PO}_4^{3-}$) and pyrophosphate ($\text{Q}^1\text{P}_2\text{O}_7^{4-}$) units. The low intensity of the spinning sidebands suggests that the glasses are dominated by the former species possessing a characteristically low chemical shielding anisotropy (CSA). The spectra show no systematic dependence of the T_0 values but remain constant under the given synthetic parameters. Contrary to the U400 sample, the spectrum of S400 ex-

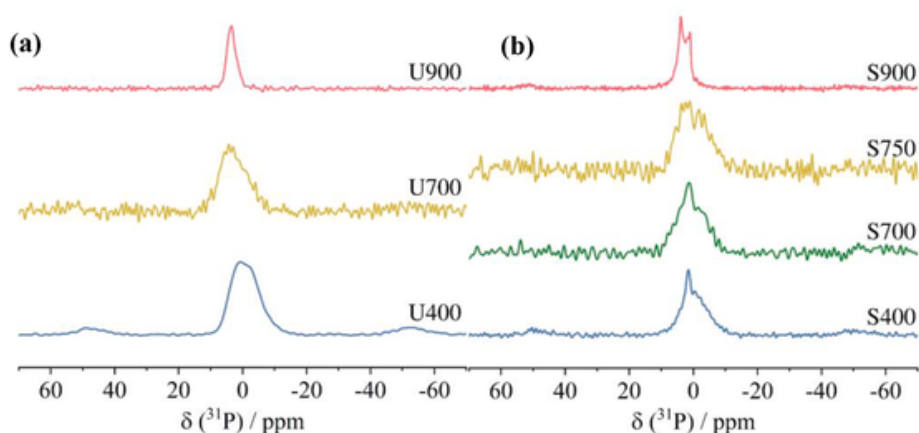


Fig. 16. ^{31}P MAS NMR spectra of the samples. Spectral deconvolutions of all spectra are shown in Fig. S6, except for U900 and S750 samples in which the experimental spectra were replaced by higher quality data recorded at a lower field (refer to Table 2 for the employed acquisition parameters).

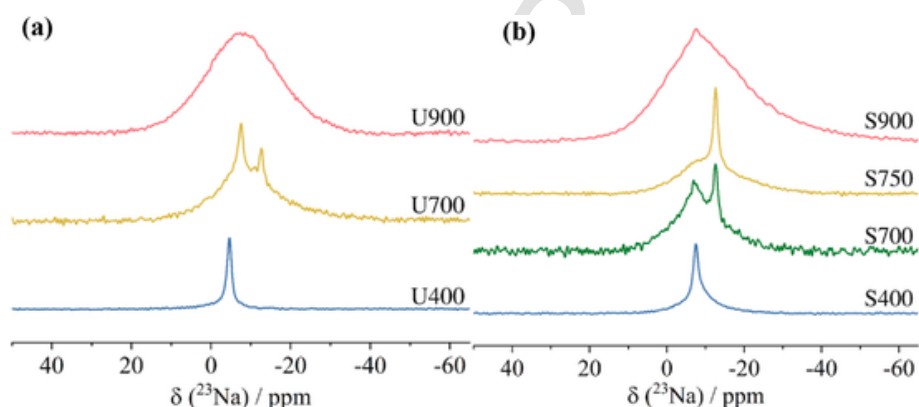


Fig. 17. ^{23}Na MAS NMR spectra of the samples. Spectral deconvolutions of all spectra are shown in Fig. S6, except for U900 and S750 samples in which the experimental spectra were replaced by higher quality data recorded at a lower field (refer to Table 2 for the employed acquisition parameters).

hibits an additional narrow signal at 1.6 ppm, possibly caused by minor amounts of unreacted H_3PO_4 or crystallization of a small part of the phosphorus oxide inventory. Similarly, two separate sharp signals can be identified for U900 and S900 samples, where the latter provides significantly less structure. The onset temperature of this narrowing above 750 °C coincides with the narrowing of B_a^3 species and strongly implies that the glasses begin to crystallize at T_0 temperatures above 750 °C.

3.6.3. ^{23}Na MAS NMR

The ^{23}Na MAS NMR spectra of the samples are shown in Fig. 17. The spectra exhibit multiple narrow features, while an additional wide feature can be found at higher T_0 values. The latter indicates ^{23}Na spins subjected to a wide distribution of EFGs. The broad line-shapes components can be well simulated using the Czjzek distribution model of quadrupolar interaction parameters confirming a high degree of disorder in those samples. For T_0 values below 750 °C, significant amounts of ^{23}Na in highly ordered environments are observed with isotropic chemical shifts of -4.6 ppm (in the U400 sample), -7.5 ppm (in S400, S700, U700, and S900 samples), and -12.6 ppm (in S700, S750, and U700 samples). For the T_0 value of 750 °C, sharp signals are absent. It is worth mentioning that the broad tail of the peak observed for the U400 sample is attributable to a weak glassy signal at $\delta_{\text{iso}} = -7.5$ ppm. Since the boron species found in U400 seem predominately crystalline, the ^{23}Na signals are not likely attributable to sodium borate species. On the other hand, the sharp features near -7.5 ppm indicate the presence of a minor crystalline phase, most likely owing to the sodium nitrate signal at $\delta_{\text{iso}} = -2.1$ ppm overlapping with the crystalline precursor. While it was

impossible to identify the other minority phases, the narrow signals confirm the formation of sodium phosphates which are challenging to identify based on isotropic chemical shifts alone. A preliminary ^1H NMR measurement (data not shown) confirms the presence of the strongly broadened proton signals at 4.3 ppm, which is not significantly diminished by heating at 210 °C for four days. Thus, neither hydration nor protonation of the observed crystalline ^{23}Na species can be ruled out [60].

4. Conclusion

The feasibility of producing 1393-B3 glass powders by the SCS method using different fuels was demonstrated in the present contribution. The physical and structural properties of the final glass powders synthesized at various furnace temperatures T_0 were assessed by XRD, SEM, DTA-TG, RAMAN, FTIR, and solid-state MAS-NMR techniques. The results indicate that using sucrose and urea as fuels can obtain glassy porous powders over an extensive temperature range ranging from about 400 to 750 °C and 500–700 °C. The DTA-TG results, jointly with thermodynamic calculations and NMR results, indicate that the glass transition temperatures are affected by the synthesis temperature. Conducting the synthesis process using urea at lower furnace temperatures leaves significant amounts of precursors behind and produces crystalline borate phases as detected via ^{11}B MAS NMR. On the other hand, for samples produced near the optimum T_0 values, the absence of narrow signals in the ^{31}P and ^{11}B MAS NMR spectra confirms that no crystalline impurity phases are present in the glass network. Furthermore, according to ^{11}B MAS NMR, distinct neutral (B^{3n}) and anionic

(B^{3a}, B⁴) borate units are present as the local structural groups in the glass powders. The amount of four-coordinated boron (N_4) decreased from about 60 to 35% by increasing the T_0 values, while the overall amount of the neutral B³ⁿ species stayed nearly constant. Future studies should be aimed at further understanding the microstructure of the produced materials and further improving the synthesis process by discussing possible application scenarios. Currently, in-depth structural analyses and bioactivity tests of the synthesized 1393-B3 glass powders through advanced solid-state NMR methods and relative biocompatibility and bioactivity assessments are currently underway in our laboratories.

Uncited references

[61]; [62].

Declaration of competing interest

The authors declare that they have no known competing financial interests or personal relationships that could have appeared to influence the work reported in this paper.

Acknowledgments

M.G. acknowledges financial support from Ferdowsi University of Mashhad, Iran (No. 3/55475). H.B. gratefully acknowledges FAPESP for a personal post-doctoral stipend under grant No. 2019/26399–3. Finally, the authors thank Prof. Dr. Hellmut Eckert (Physics Institute, USP, São Carlos, Brazil) for valuable discussions regarding the structural interpretation of the ¹¹B NMR data.

Appendix A. Supplementary data

Supplementary data to this article can be found online at <https://doi.org/10.1016/j.ceramint.2023.01.061>.

References

- S. Kargozar, R.K. Singh, H.W. Kim, F. Baino, Hard” ceramics for “Soft” tissue engineering: paradox or opportunity? *Acta Biomater.* 115 (2020), <https://doi.org/10.1016/j.actbio.2020.08.014>.
- P. Tomlins, Material types for tissue scaffolds, in: *Characterisation Des. Tissue Scaffolds*, 2016, <https://doi.org/10.1016/B978-1-78242-087-3.00001-8>.
- Q. Fu, M.N. Rahaman, H. Fu, X. Liu, Silicate, borosilicate, and borate bioactive glass scaffolds with controllable degradation rate for bone tissue engineering applications. I. Preparation and in vitro degradation, *J. Biomed. Mater. Res., Part A* 95 (2010), <https://doi.org/10.1002/jbm.a.32824>.
- Y. Tang, L. Pang, D. Wang, Preparation and characterization of borate bioactive glass cross-linked PVA hydrogel, *J. Non-Cryst. Solids* 476 (2017), <https://doi.org/10.1016/j.jnoncrysol.2017.07.017>.
- P. Balasubramanian, T. Büttner, V. Miguez Pacheco, A.R. Boccaccini, Boron-containing bioactive glasses in bone and soft tissue engineering, *J. Eur. Ceram. Soc.* 38 (2018), <https://doi.org/10.1016/j.jeurceramsoc.2017.11.001>.
- F.H. Nielsen, Is boron nutritionally relevant? *Nutr. Rev.* 66 (2008), <https://doi.org/10.1111/j.1753-4887.2008.00023.x>.
- X. Liu, M.N. Rahaman, D.E. Day, Conversion of melt-derived microfibrillar borate (13-93B3) and silicate (45S5) bioactive glass in a simulated body fluid, *J. Mater. Sci. Mater. Med.* 24 (2013), <https://doi.org/10.1007/s10856-012-4831-z>.
- T.A. Taha, Y.S. Rammah, Optical characterization of new borate glass doped with titanium oxide, *J. Mater. Sci. Mater. Electron.* 27 (2016), <https://doi.org/10.1007/s10854-015-3901-7>.
- T. Mehrabi, A.S. Mesgar, Z. Mohammadi, Bioactive glasses: a promising therapeutic ion release strategy for enhancing wound healing, *ACS Biomater. Sci. Eng.* 6 (2020) 5399–5430.
- J. Zhou, H. Wang, S. Zhao, N. Zhou, L. Li, W. Huang, D. Wang, C. Zhang, In vivo and in vitro studies of borate based glass micro-fibers for dermal repairing, *Mater. Sci. Eng. C* 60 (2016), <https://doi.org/10.1016/j.msec.2015.11.068>.
- G. Kaur, G. Pickrell, N. Sriranganathan, V. Kumar, D. Homa, Review and the state of the art: sol–gel and melt quenched bioactive glasses for tissue engineering, *J. Biomed. Mater. Res. Part B Appl. Biomater.* 104 (2016), <https://doi.org/10.1002/jbm.b.33443>.
- G. Kaur, G. Pickrell, G. Kimsawatde, D. Homa, H.A. Allbee, N. Sriranganathan, Synthesis, cytotoxicity, and hydroxyapatite formation in 27-Tris-SBF for sol-gel based CaO-P2O5-SiO2-B2O 3-ZnO bioactive glasses, *Sci. Rep.* 4 (2014), <https://doi.org/10.1038/srep04392>.
- G. Kaur, O.P. Pandey, K. Singh, D. Homa, B. Scott, G. Pickrell, A review of bioactive glasses: their structure, properties, fabrication and apatite formation, *J. Biomed. Mater. Res., Part A* 102 (2014), <https://doi.org/10.1002/jbm.a.34690>.
- J. Chevalier, L. Gremillard, Ceramics for medical applications: a picture for the next 20 years, *J. Eur. Ceram. Soc.* 29 (2009), <https://doi.org/10.1016/j.jeurceramsoc.2008.08.025>.
- W.C. Lepry, S.N. Nazhat, Highly bioactive sol-gel-derived borate glasses, *Chem. Mater.* 27 (2015), <https://doi.org/10.1021/acs.chemmater.5b01697>.
- W.C. Lepry, S.N. Nazhat, A review of phosphate and borate sol-gel glasses for biomedical applications, *Adv. NanoBiomed. Res.* 1 (2021), <https://doi.org/10.1002/anbr.202000055>.
- J.H. Lopes, O.M.V.M. Bueno, I.O. Mazali, C.A. Bertran, Investigation of citric acid-assisted sol-gel synthesis coupled to the self-propagating combustion method for preparing bioactive glass with high structural homogeneity, *Mater. Sci. Eng. C* 97 (2019), <https://doi.org/10.1016/j.msec.2018.12.022>.
- A. Varma, A.S. Mukasyan, A.S. Rogachev, K.V. Manukyan, Solution combustion synthesis of nanoscale materials, *Chem. Rev.* 116 (2016), <https://doi.org/10.1021/acs.chemrev.6b00279>.
- A.V. Saghir, S.M. Beidokhti, J.V. Khaki, A. Salimi, One-step synthesis of single-phase (Co, Mg, Ni, Cu, Zn) O High entropy oxide nanoparticles through SCS procedure: thermodynamics and experimental evaluation, *J. Eur. Ceram. Soc.* 41 (2021), <https://doi.org/10.1016/j.jeurceramsoc.2020.08.044>.
- E.G. Nezhad, S.M. Beidokhti, J. Vahdati-Khaki, Accelerated crystallization of CuAlO2 delafossite phase by controlling thermal regime during solution combustion synthesis, *Ceram. Int.* 46 (2020), <https://doi.org/10.1016/j.ceramint.2020.05.040>.
- H. Aali, S. Mollazadeh, J.V. Khaki, Single-phase magnetite with high saturation magnetization synthesized via modified solution combustion synthesis procedure, *Ceram. Int.* (2018), <https://doi.org/10.1016/j.ceramint.2018.08.012>.
- Z. Mollaei, F. Kermani, F. Moosavi, S. Kargozar, J.V. Khaki, S. Mollazadeh, In silico study and experimental evaluation of the solution combustion synthesized manganese oxide (MnO2) nanoparticles, *Ceram. Int.* 48 (2022), <https://doi.org/10.1016/j.ceramint.2021.09.245>.
- M. Huang, M. Qin, P. Chen, B. Jia, Z. Chen, R. Li, Z. Liu, X. Qu, Facile preparation of network-like porous hematite (α-Fe2O3) nanosheets via a novel combustion-based route, *Ceram. Int.* 42 (2016), <https://doi.org/10.1016/j.ceramint.2016.03.175>.
- A. Roine, HSC chemistry®, www.outotec.com/HSC, 2019.
- J.A. Dean, *Lange's Handbook of Chemistry*, fifteenth ed., 1999.
- S.G.J. van Meerten, W.M.J. Franssen, A.P.M. Kentgens, ssNake, A cross-platform open-source NMR data processing and fitting application, *J. Magn. Reson.* 301 (2019), <https://doi.org/10.1016/j.jmr.2019.02.006>.
- G. Le Caër, B. Bureau, D. Massiot, An extension of the Czjzek model for the distributions of electric field gradients in disordered solids and an application to {NMR} spectra of 71Ga in chalcogenide glasses, *J. Phys. Condens. Matter* 22 (2010) 65402, <https://doi.org/10.1088/0953-8984/22/6/065402>.
- G. Czjzek, J. Fink, F. Götz, H. Schmidt, J.M.D. Coey, J.P. Rebouillat, A. Liénard, Atomic coordination and the distribution of electric field gradients in amorphous solids, *Phys. Rev. B* 23 (1981), <https://doi.org/10.1103/PhysRevB.23.2513>.
- D. Marion, M. Ikura, R. Tschudin, A. Bax, Rapid recording of 2D NMR spectra without phase cycling. Application to the study of hydrogen exchange in proteins, *J. Magn. Reson.* 85 (1989), [https://doi.org/10.1016/0022-2364\(89\)90152-2](https://doi.org/10.1016/0022-2364(89)90152-2).
- J.P. Amoureux, C. Fernandez, S. Steuernagel, Z filtering in MQMAS NMR, *J. Magn. Reson. A* 123 (1996) 116–118, <https://doi.org/10.1006/jmra.1996.0221>.
- E. Novitskaya, J.P. Kelly, S. Bhaduri, O.A. Graeve, A review of solution combustion synthesis: an analysis of parameters controlling powder characteristics, *Int. Mater. Rev.* 66 (2021), <https://doi.org/10.1080/09506608.2020.1765603>.
- T.N.H. Tengku Kamarul Bahri, R. Hussin, N.E. Ahmad, Thermoluminescence studies of calcium metaborate (CaB2O4) nanocrystals synthesized by solution combustion method, *Malaysian J. Fundam. Appl. Sci.* 13 (2017), <https://doi.org/10.11113/mjfas.v0n0.580>.
- I. Charak, M. Manhas, P. Khajuria, A.K. Bedyal, H.C. Swart, V. Kumar, Investigation of thermoluminescence response and kinetic parameters of CaMgB2O5: Tb3+ phosphor against UV-C radiation for dosimetric application, *J. Mater. Sci. Mater. Electron.* 32 (2021), <https://doi.org/10.1007/s10854-021-06273-y>.
- H. Aali, S. Mollazadeh, J.V. Khaki, Quantitative evaluation of ambient O2 interference during solution combustion synthesis process: considering iron nitrate – fuel system, *Ceram. Int.* 45 (2019), <https://doi.org/10.1016/j.ceramint.2019.05.348>.
- N.J. Baygi, A.V. Saghir, S.M. Beidokhti, J.V. Khaki, Modified auto-combustion synthesis of mixed-oxides TiO2/NiO nanoparticles: physical properties and photocatalytic performance, *Ceram. Int.* 46 (2020), <https://doi.org/10.1016/j.ceramint.2020.03.087>.
- Q. Jiao, G. Li, D. Zhou, J. Qiu, Effect of the glass structure on emission of rare-earth-doped borate glasses, *J. Am. Ceram. Soc.* 98 (2015), <https://doi.org/10.1111/jace.13832>.
- J.E. Shelby, *Introduction to Glass Science and Technology*, second ed., 2005.
- M.J. Snyder, M.G. Mesko, J.E. Shelby, Volatilization of boron from E-glass melts, *J. Non-Cryst. Solids* 352 (2006), <https://doi.org/10.1016/j.jnoncrysol.2005.11.068>.
- F.D. Haghighi, S.M. Beidokhti, Z.T. Najaran, S. Sahebian Saghi, Highly improved biological and mechanical features of bioglass-ceramic/gelatin composite scaffolds using a novel silica coverage, *Ceram. Int.* 47 (2021), <https://doi.org/10.1016/j.ceramint.2021.01.274>.

- [40] G. Rytwo, R. Zakai, B. Wicklein, The use of ATR-FTIR spectroscopy for quantification of adsorbed compounds, *J. Spectrosc.* (2015) <https://doi.org/10.1155/2015/727595>, 2015.
- [41] F.H. El-Batal, A.A. El-Khesheh, G.T. El-Bassyouni, A.A. Abd El Aty, In vitro bioactivity behavior of some borate glasses and their glass-ceramic derivatives containing Zn^{2+} , Ag^+ or Cu^{2+} by immersion in phosphate solution and their anti-microbial activity, *Silicon* 10 (2018), <https://doi.org/10.1007/s12633-017-9552-y>.
- [42] A.O. Surendranathan, An introduction to ceramics and refractories, <https://doi.org/10.1201/b17811>, 2014.
- [43] S. Mondal, A.K. Banthia, Low-temperature synthetic route for boron carbide, *J. Eur. Ceram. Soc.* 25 (2005), <https://doi.org/10.1016/j.jeurceramsoc.2004.08.011>.
- [44] H.D. Shashikala Subhashini, N.K. Udayashankar, Investigation of mixed alkali effect on mechanical, structural and thermal properties of three-alkali borate glass system, *J. Alloys Compd.* 658 (2016), <https://doi.org/10.1016/j.jallcom.2015.11.014>.
- [45] A. Yao, M.N. Rahaman, J. Lin, W. Huang, Structure and crystallization behavior of borate-based bioactive glass, *J. Mater. Sci.* (2007), <https://doi.org/10.1007/s10853-007-1995-x>.
- [46] K. Li, W. Cai, Z. Zhang, H. Xie, Q. Zhong, H. Qu, Boron doped C3N5 for photocatalytic nitrogen fixation to ammonia: the key role of boron in nitrogen activation and mechanism, *Chem. Eng. J.* 435 (2022) 135017.
- [47] M.H. Brooker, D.E. Irish, Infrared and Raman spectral studies of KNO₂–KNO₃ solutions, *Can. J. Chem.* 46 (1968) 229–233.
- [48] Y. Chen, C. Zou, M. Mastalerz, S. Hu, C. Gasaway, X. Tao, Applications of micro-fourier transform infrared spectroscopy (FTIR) in the geological sciences—a Review, *Int. J. Mol. Sci.* 16 (2015), <https://doi.org/10.3390/ijms161226227>.
- [49] M. Nedyalkova, H. Hristov, V. Simeonov, Statistical approach to study of lithium magnesium metaborate glasses, *Open Chem* 15 (2017), <https://doi.org/10.1515/chem-2017-0008>.
- [50] A.K. Yadav, P. Singh, A review of the structures of oxide glasses by Raman spectroscopy, *RSC Adv.* 5 (2015), <https://doi.org/10.1039/c5ra13043c>.
- [51] K. Schuhladen, U. Pantulap, K. Engel, P. Jeleń, Z. Olejniczak, L. Hupa, M. Sitarz, A.R. Boccaccini, Influence of the replacement of silica by boron trioxide on the properties of bioactive glass scaffolds, *Int. J. Appl. Glass Sci.* 12 (2021), <https://doi.org/10.1111/ijag.15894>.
- [52] P. Stoch, P. Goj, M. Ciecinska, A. Stoch, Structural features of 19Al₂O₃–19Fe₂O₃–62P₂O₅ glass from a theoretical and experimental point of view, *J. Non-Cryst. Solids* 521 (2019), <https://doi.org/10.1016/j.jnoncrysol.2019.119499>.
- [53] S. Kroeker, J.F. Stebbins, Three-coordinated boron-11 chemical shifts in borates, *Inorg. Chem.* 40 (2001) 6239–6246, <https://doi.org/10.1021/ic010305u>.
- [54] P.M. Aguiar, S. Kroeker, Boron speciation and non-bridging oxygens in high-alkali borate glasses, *J. Non-Cryst. Solids* 353 (2007), <https://doi.org/10.1016/j.jnoncrysol.2007.02.013>.
- [55] G.-C. Guo, W.-D. Cheng, J.-T. Chen, J.-S. Huang, Q.-E. Zhang, Triclinic Mg₂B₂O₅, *Acta Crystallogr. Sect. C Cryst. Struct. Commun.* 51 (1995) 351–353.
- [56] T. Jin, G.M. Bernard, M. Miskolzie, V. V Terskikh, V.K. Michaelis, A 11B and 31P MAS NMR study of the impact of Ca²⁺ and Sr²⁺ network modifying cations on the structure of borate and borophosphate glasses, *Phys. Chem. Glas. J. Glas. Sci. Technol. Part B.* 59 (2018) 174–180.
- [57] J. Wu, J.F. Stebbins, Effects of cation field strength on the structure of aluminoborosilicate glasses: high-resolution 11B, 27Al and 23Na MAS NMR, *J. Non-Cryst. Solids* 355 (2009), <https://doi.org/10.1016/j.jnoncrysol.2009.01.025>.
- [58] T. Bauer, D. Laing, R. Tamme, Characterization of sodium nitrate as phase change material, *Int. J. Thermophys.* 33 (2012), <https://doi.org/10.1007/s10765-011-1113-9>.
- [59] X. Jiao, Y. Liu, X. Cai, J. Wang, P. Feng, Progress of porous Al-containing intermetallics fabricated by combustion synthesis reactions: a review, *J. Mater. Sci.* 56 (2021) 11605–11630.
- [60] K.J.D. MacKenzie, M.E. Smith, *Multinuclear Solid-State Nuclear Magnetic Resonance of Inorganic Materials*, 2002.
- [61] J.J. Moore, H.J. Feng, Combustion synthesis of advanced materials: Part I. Reaction parameters, *Prog. Mater. Sci.* 39 (1995) 243–273, [https://doi.org/10.1016/0079-6425\(94\)00011-5](https://doi.org/10.1016/0079-6425(94)00011-5).
- [62] T. Langner, A. Rietig, J. Acker, Raman spectroscopic determination of the degree of dissociation of nitric acid in binary and ternary mixtures with HF and H₂SiF₆, *J. Raman Spectrosc.* 51 (2020), <https://doi.org/10.1002/jrs.5769>.